Disk-jet coupling across the spectral transition in supermassive black holes

Jia-Lai Kang[1,2,3]★, Chris Done[1,4]†, Scott Hagen[1], Mai Liao[5], Matthew J. Temple[1], John D. Silverman[4,6,7,8], Junyao Li[9], Jun-Xian Wang[2,3]

[1]Centre for Extragalactic Astronomy, Department of Physics, Durham University, South Road, Durham, DH1 3LE, UK
[2]Department of Astronomy, University of Science and Technology of China, Hefei 230026, China
[3]School of Astronomy and Space Science, University of Science and Technology of China, Hefei 230026, China
[4]Kavli Institute for the Physics and Mathematics of the Universe (Kavli IPMU, WPI), UTIAS, Tokyo Institutes for Advanced Study, University of Tokyo, Chiba, 277-8583, Japan
[5]Universidad Diego Portales, Av Republica 180, Santiago, Regiún Metropolitana, Chile
[6]Department of Astronomy, School of Science, The University of Tokyo, 7-3-1 Hongo, Bunkyo, Tokyo 113-0033, Japan
[7]Center for Data-Driven Discovery, Kavli IPMU (WPI), UTIAS, The University of Tokyo, Kashiwa, Chiba, 277-8583, Japan
[8]Center for Astrophysical Science, Department of Physics & Astronomy, John Hopkins University, Baltimore, MD 21218, USA
[9]Department of Astronomy, Univerity of Illinois at Urbana-Champaign, Urbana, IL 61801, USA

Accepted XXX. Received YYY; in original form ZZZ

ABSTRACT

Accretion flows in both stellar and supermassive black holes show a distinct spectral transition. This is seen directly in binaries and changing look AGN, and also in a recent sample of eROSITA X-ray selected, unobscured AGN where the stacked spectral energy distributions (SEDs) for a single black hole mass bin ($\log M/M_\odot = 8-8.5$) clearly show the UV bright disk appearing as the luminosity increases. In binaries, this transition is associated with a change in radio jet, from coupling to the X-ray hot flow with $L_R \propto L_X^{0.7}$ (Fundamental Plane relation), to collapsing when the X-ray hot flow collapses into a disc. We explore the radio behaviour across the transition in our AGN sample by stacking VLASS images. We significantly detect weak radio emission even after subtracting the contribution from star formation in the host galaxy. The residual radio emission remains relatively constant across the transition, despite the mean mass accretion rate changing by a factor 6 and UV flux changing by a factor 100. However, the X-rays change by only a factor 2, giving a constant radio to X-ray flux ratio as predicted by the 'fundamental plane'. We show that this is consistent with these AGN having the same compact radio jet coupling to the X-ray hot flow (not the disc) as in the binaries. The most significant difference is the persistance of the coronal X-rays across the spectral transition in AGN, whereas in binaries the coronal X-rays can be very weak in the disc dominated state.

Key words: accretion, accretion discs – black hole physics – galaxies: active

1 INTRODUCTION

Accretion flows onto stellar mass black hole binary systems (BHXRBs) show a remarkable spectral transition, from being dominated by an optically thick thermal component peaking at 1–2 keV at high luminosity (soft state), to optically thin, Comptonised emission peaking at 100 keV at lower luminosity (hard state). This is most easily interpreted as a change in the nature and geometry of the accretion flow, from a standard disc to a radiatively inefficient/advection dominated accretion flow (ADAF/RIAF), especially as this transition occurs at $\sim 0.01 L_{\rm Edd}$ for a slow change in mass accretion rate (Maccarone 2003; Vahdat Motlagh et al. 2019), which is the maximum luminosity for an ADAF (Narayan & Yi 1994). Unlike the thermal disc, whose temperature changes with black hole mass at a given Eddington fraction ($L/L_{\rm Edd}$), the ADAF properties are mostly scale invariant. This predicts the transition should be present at similar luminosity in the accretion flows of the supermassive black holes which power AGN and Quasars (Narayan & Yi 1994). There is clear evidence for this in the "Changing Look" AGN, where a single AGN fades or brightens, giving a change in the broad band ionizing spectral energy distribution and consequent broad line emission as it crosses this luminosity (Noda & Done 2018; Ruan et al. 2019; Zeltyn et al. 2024; Jana et al. 2025). Nonetheless, these are rare systems (e.g., Temple et al. 2023). More compelling evidence would be to see this transition in the broader population. However, this is difficult as an AGN dims towards $L \sim 0.01 L_{\rm Edd}$ as the host galaxy emission becomes more important, and the visibility of a UV disc and broad line region can be easily suppressed through obscuration. Recently, these issues were tackled in Hagen et al. (2024) by building a new X-ray selected sample from eROSITA (Brunner et al. 2022; Liu et al. 2022), with $N_{\rm H} < 10^{22}$ cm^{-2} such that reddening associated with cold gas is small. This was crossmatched with galaxies imaged in the HyperSuprime Cam field (Aihara et al. 2022; Li et al. 2024),

★ jialai.kang@durham.ac.uk
† chris.done@durham.ac.uk

so that the extended host galaxy emission could be modelled and subtracted. The host stellar mass also gave an estimate for black hole mass across the entire sample, removing the requirement that the broad emission lines are detected. Selecting only a single mass bin ($\log M_{\rm BH}/M_{\odot} = 8.0 - 8.5$) clearly shows that the emission from a blue optically thick disk–like flow collapses at $L \sim 0.01 L_{\rm Edd}$ in the entire population (Hagen et al. 2024) and that this has even more impact on the UV emission and its reprocessing into broad emission lines (BLR) (Kang et al. 2025).

In binaries, this spectral transition is associated with a dramatic change in the radio emission. The radio flux from the compact steady jet correlates with the X-ray emission from the hot flow in the hard states, with $L_{\rm R} \propto L_{\rm X}^{0.7}$ (see e.g. Corbel et al. 2013). This correlation breaks down at the hard-soft transition, where discrete ballistic jet ejections dominate the radio (see e.g. Gallo et al. 2003). The correlation also breaks down after the transition, where the X-rays in BHXRBs are dominated by the disc component (Gallo et al. 2003; Fender et al. 2004). This shows that the radio emission correlates with the X-ray hot coronal flux, and not with the total mass accretion rate which powers the disc component. This is consistent with models where the X-ray hot flow not the thin disc connects to the jet, plausibly because the flow has large scale height so supports large scale height magnetic fields which provide the poloidal component close to the black hole which powers the jet. The radio can then be produced by the sum of self-absorbed synchrotron emission components from a vertically extended Blandford & Königl (1979) conical jet (Merloni et al. 2003; Heinz & Sunyaev 2003). This predicts a 'fundamental plane of radio-X-ray emission' (hereafter FP) for the hard state emission where $\log L_{\rm R} = 0.7 \log L_{\rm X} + 0.7 \log M + C$, connecting across from BHXRBs to AGN (see §2.3). The mass dependence is important as the BHXRBs all have similar black hole masses (within a factor 2–3), which reveals the correlation directly, but AGN span from $10^5 - 10^{10} M_{\odot}$, which leads to considerable scatter in a direct correlation (Merloni et al. 2003).

Multiple studies have tried to associate the very wide range of radio behaviour seen in AGN with this complex behaviour seen in the BHXRBs states (Körding et al. 2006; Sobolewska et al. 2011; Svoboda et al. 2017; Fernández-Ontiveros & Muñoz-Darias 2021; Moravec et al. 2022). A small fraction ($\sim 10\%$) of AGN have powerful relativistic jets, but unlike BHXRBs jets (either compact or ballistic), these have high bulk Lorentz factor of $\sim 10 - 20$ (Ghisellini et al. 2010). This means that the jet emission is strongly beamed and dominates the radio and X-ray bandpasses where the jet aligns with the line of sight (Blazars: BL Lacs and Flat spectrum radio sources: FSRQ). The relativistic jet is still clearly evident when sources are misaligned, as it powers strong radio emitting extended structures (Fanaroff-Riley types 1 and 2, Urry & Padovani 1995). However, most AGN do not have such large scale/high bulk Lorentz factor/high power jets, but do have compact emission which could be from a steady jet such as is seen in the hard state BHXRBs (Falcke & Biermann 1995; Giroletti & Panessa 2009; Panessa & Giroletti 2013). However, this origin is controversial as there could also be contributions from shocks from AGN winds (Zakamska & Greene 2014; Nims et al. 2015; Chen et al. 2024), or radio emission from the X-ray coronae itself (Laor & Behar 2008; Behar et al. 2015; Chen et al. 2023), and/or star formation processes (Condon 1992; Thean et al. 2001; Delvecchio et al. 2017). See e.g. Panessa et al. (2019) for a review.

The distinction between sources with and without a high Lorentz factor relativistic jet seems more robust than the radio-loud (RL) / radio-quiet (RQ) distinction. Radio-loudness R, is defined as the ratio between the radio and optical fluxes (e.g., Kellermann et al. 1989), with $R = 10$ used as the boundary. AGN with a powerful relativistic jet are indeed very RL, but the drop in optical luminosity at the spectral transition could also lead to a compact jet with much smaller radio luminosity/smaller bulk Lorentz factor like that of the BHXRBs being classed as RL (Körding et al. 2006; Sobolewska et al. 2011; Svoboda et al. 2017).

Here we take the single mass range AGN sample of Hagen et al. (2024); Kang et al. (2025) and extend the SEDs into the radio band to investigate the effect of the spectral transition on the properties of the jet. Only 29/1305 of our sources are detected individually (these are RL) so we stack the undetected sources into three bins of increasing $\dot{m} = L/L_{\rm Edd}$ (defined by the optical/UV/X-ray SEDs) to explore their faint radio emission. We subtract the radio emission from a matched host galaxy sample, and find that the residual radio emission is relatively constant, despite spanning the spectral transition. The mass accretion rate changes by a factor 6 from the first bin below the spectral transition to the brightest bin, and there is a factor 100 change in UV flux. However, the coronal X-ray luminosity changes by less than a factor 2 across the SEDs, unlike the BHXRBs where the coronal X-ray luminosity can drop to very low values after the transition. The lack of change in radio emission is then consistent with the (lack of) change in X-ray emission, and the resulting radio-X-ray ratio is broadly consistent with the FP relation of Merloni et al. (2003), but the large change in optical/UV means that the stacked spectra switch from RL to RQ across the spectral transition. This shows that the FP i.e. radio to X-ray ratio, gives more insight into the jet properties in AGN than the classical radio to optical ratio, again showing that, similar to the BHXRBs, the radio follows the X-ray corona rather than the total mass accretion rate. Thus the term 'disk-jet' coupling which is often used in the literature is a somewhat of a misnomer, as the jet couples with the X-ray hot flow, not to the optically thick disc.

This supports FP models where the origin of the radio emission in these RQ AGN is from a low power, steady compact jet with low/moderate bulk Lorentz factor, which couples to the X-ray emitting accretion flow in a similar way to that seen in the stellar mass black hole binaries.

There are some differences though: in the stellar mass BHXRBs the X-ray coronal emission can be very low after the transition, while in AGN the X-ray flux stays at roughly the level of the brightest ADAF (Kubota & Done 2018). Another difference is that the AGN clearly show very significant dispersion with respect to the FP, with a tail to higher core radio to X-ray ratios. We suggest that distance from the FP is a better way to characterise strong jet power sources, and speculate that this is due to some AGN reaching higher black hole spins than BHXRBs due to their very different formation and evolution histories.

2 EFEDS-HSC SAMPLE

2.1 Stacked VLASS images

The eFEDS field is fully covered by the Karl G. Jansky Very Large Array Sky Survey (VLASS, Lacy et al. 2020). This radio survey is conducted with the NRAO Very Large Array (VLA) in its B-configuration within 2–4 GHz band. VLASS images have a pixel size of 1.0″, spatial resolution of 2.5″, and a typical rms of 120 μJy beam^{-1} for a single-epoch image. All the three epoch Quick Look images of the eFEDS field have now been released, giving a combined typical rms of ~ 70 μJy beam^{-1}. For each source, we download the three epoch cut-out images from the Canadian Astronomy Data Centre (CASC) database, with a size of 81×81 arcsec^2.

For each source, we median stack the three VLASS images and perform the source detection on the stacked image. We adopt a simple criterion for detection, i.e., the peak flux within the center $3'' \times 3''$ area is larger than 420 μJy (the typical rms of a stacked image is 69 μJy, thus $\sim 6\sigma$ level). By combining the three epoch images, we detect 29 sources, 16 of which are in the VLASS Quick Look epoch 1 catalog. Most of them are point-like sources as shown in Figure A2, and most are radio-loud with radio loudness $R > 10$, where $R = \frac{f_{5\ \mathrm{GHz}}}{f_{2500\text{Å}}}$ (e.g., Kellermann et al. 1989; Schulze et al. 2017). These detected sources are fairly evenly distributed across the sample in terms of $\dot{m}$ (see Figure A2), with detection rates of 2.9%, 2.0% and 2.3%, respectively. This is substantially below the often quoted $\sim$ 10% of AGN being RL. The VLASS flux limits predicted from the SEDs are 243, 39 and 6 μJy for $R = 10$ at the mean redshift, for bright, middle and faint bins respectively, so we could be missing some RL sources, especially in the fainter bins.

We visually inspect all the remaining sources, and find 55 with contamination from nearby sources or spurious features (see Figure A3). These 84 sources (detected and contaminated) are excluded from the remaining analysis.

We then stack the remaining undetected source cut-out images following the procedure in Liao et al. (2022, 2024). In brief, we align and median stack the cutouts on a pixel-by-pixel basis to obtain a stacked image (e.g., White et al. 2007; Fawcett et al. 2020). Median stacking is less sensitive to outliers (e.g., a small fraction of more radio-loud objects despite our removal of all detected sources) compared with mean stacking. Since the varying point-spread-functions (PSFs) of the VLASS images have not been CLEANed, we only adopt the peak flux density from the central pixel in each stacked image, where the nominal point-like sources should be centered (White et al. 2007), as an average radio flux for analysis, and we use the bootstrapping method in Karim et al. (2011) to derive uncertainties.

To achieve high enough signal-to-noise ratios, we rebin the original eight luminosity bins in Hagen et al. (2024); Kang et al. (2025) into three bins, faint (νL_{3500} in [42.1, 43.3], 469 sources, top row), middle (νL_{3500} in [43.3, 44.1], 580 sources, 2 out of 3 middle row) and bright (νL_{3500} in [44.1, 45.3], 256 sources, bottom row and the brightest middle row bin). In Figure A1 we show the re-binned SED of the three bins. Instead of re-fitting the data, we simply calculate the mean data, best-fit model and accretion rate $\dot{m}$ by averaging the corresponding bins, weighted by their source numbers. It is clear that the disky warm Comptonization emission (green dashed line) is very different in the three bins, while the hard X-ray luminosity (integration of the blue dashed line) remains similar, despite a systematic change in spectral slope.

The stacked VLASS images are shown in Figure 2. For all the three luminosity bins, we detect a signal at $> 5\sigma$ level. Strikingly, the radio fluxes are statistically the same among the three bins, despite their vastly different optical/UV to X-ray SEDs.

This could be explained if the radio follows the X-ray flux, rather than the total mass accretion rate, as in the stellar mass binary systems. However, the constancy of radio flux between these bins could also be explained if it is dominated by the host galaxy, as all these bins have similar host galaxy masses. To explore this, we need to estimate and subtract any host contamination before comparing the intrinsic radio luminosities.

2.2 Radio emission of host galaxies

Inactive (without an AGN) galaxies are not radio-silent. They usually show broad-band radio emission produced by synchrotron radiation and free-free emission from H II regions as well as the thermal re-radiation by dust (see the review by Condon 1992). In particular, a tight correlation between the far-infrared (FIR) and radio emission has been widely observed in star-forming galaxies (Yun et al. 2001; Sargent et al. 2010). Since the FIR emission is a direct probe of dust and cold gas, such a correlation implies the radio emission to be driven by recent star forming activities, probably synchrotron emission from supernovae shocks accelerating particles to relativistic energies.

It is not yet clear whether the radio emission in radio-quiet AGN is predominantly from the AGN nucleus or from the host galaxy. Some works have shown the host galaxy dominates (Bonzini et al. 2015; Padovani 2016), while others show an AGN-dominated (Zakamska et al. 2016; Calistro Rivera et al. 2024) or a more complicated hybrid scenario (Yue et al. 2024).

We explore this in our sample. Using the decomposed HSC images, Li et al. (2024) has classified the host galaxies in our sample into star-forming (SF) and quiescent (QS) galaxies, based on the $u - r$ versus $r - z$ diagram. As shown in Figure 3, the fractions of the SF and QS galaxies are different in the three bins and are redshift dependent. It is thus difficult to estimate the contribution of the host galaxy using known empirical correlations; instead, we attempt to build a control sample of matched inactive galaxies to quantify that.

The HSC-eFEDS sample in Kawinwanichakij et al. (2021) (hereafter K21 sample) contains more than 1 million inactive galaxies, the stellar masses and types (SF or QS) of which have been determined in the same way as our sample (Li et al. 2024), and thus can be used as a perfect control sample. In the first place we want to quantify the typical flux of the host galaxies in our sample. We randomly select 4000 SF and 4000 QS galaxies with log M_{stellar} ($M_\odot$) among 10.5–11.0 (typical values for our sample, and we will construct more strict control samples below), and with redshift evenly distributed between $z = 0.4 - 0.5$. We stack their VLASS images, as shown in Figure 4. We conclude that 1) the QS galaxies in the K21 sample classifed by color-color diagram also show some radio emission, while SF galaxies are about two times brighter; 2) both types of galaxies can contribute to a significant but not dominant fraction of the observed fluxes in our AGN sample.

We now build a matched control sample of inactive galaxies for our AGN sample. For each QS/SF host galaxy in our AGN sample, we find 10 inactive QS/SF galaxies in the K21 sample with similar redshift and M_{stellar}. Such a control sample should well represent the properties of the host galaxies in our sample, unless some key parameters (e.g., star-formation rate and size) are strongly correlated with AGN activities. The stacked VLASS images of the control sample are shown in the lower panels of Figure 2. In all the three bins, the host galaxy contributes $\lesssim$ 50 percent of the observed flux. We then adopt the host-subtracted fluxes as the intrinsic AGN radio fluxes in the following analysis. These give an upper limit to any radio emitting compact jet from the AGN, as these host subtracted radio fluxes could still be contaminated by emission from either unresolved nuclear star-formation, or shocks from AGN winds.

2.3 Radio luminosity and the fundamental plane

We convert the host-subtracted VLASS fluxes into rest-frame 5 GHz luminosities, assuming a power law spectrum with a slope $\alpha_\nu = -0.5$ (e.g., Jiang et al. 2007), and distances calculated from the mean redshift in each bin using the Planck 2018 cosmology parameters (Planck Collaboration et al. 2020). The $\nu L_{5\ \mathrm{GHz}}$ of the faint, middle and bright bins are 4.3, 6.2 and 9.6×10^{38} erg cm^{-2} s^{-1}, respectively. The bright bin is only twice as luminous as the faint bin in radio

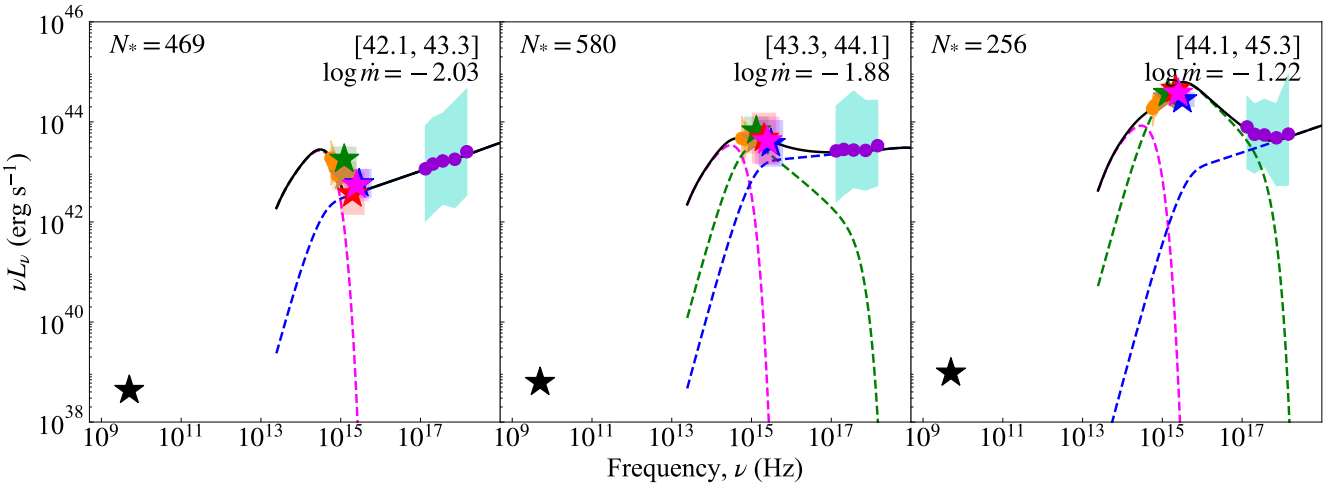

Figure 1. The stacked VLASS data (black star), along with the optical to X-ray SED in the three bins derived by averaging those in Hagen et al. (2024) and Kang et al. (2025). Each panel shows the $\nu L_{3500\text{Å}}$ luminosity bin range in the top right corner. The solid line is the best-fit AGNSED model (Kubota & Done 2018) in Hagen et al. (2024), while the dashed lines show the individual components of the standard outer disc (magenta), warm Comptonising disc (green), and inner hot X-ray plasma (blue). See Figure A1 for a detailed view of the SED.

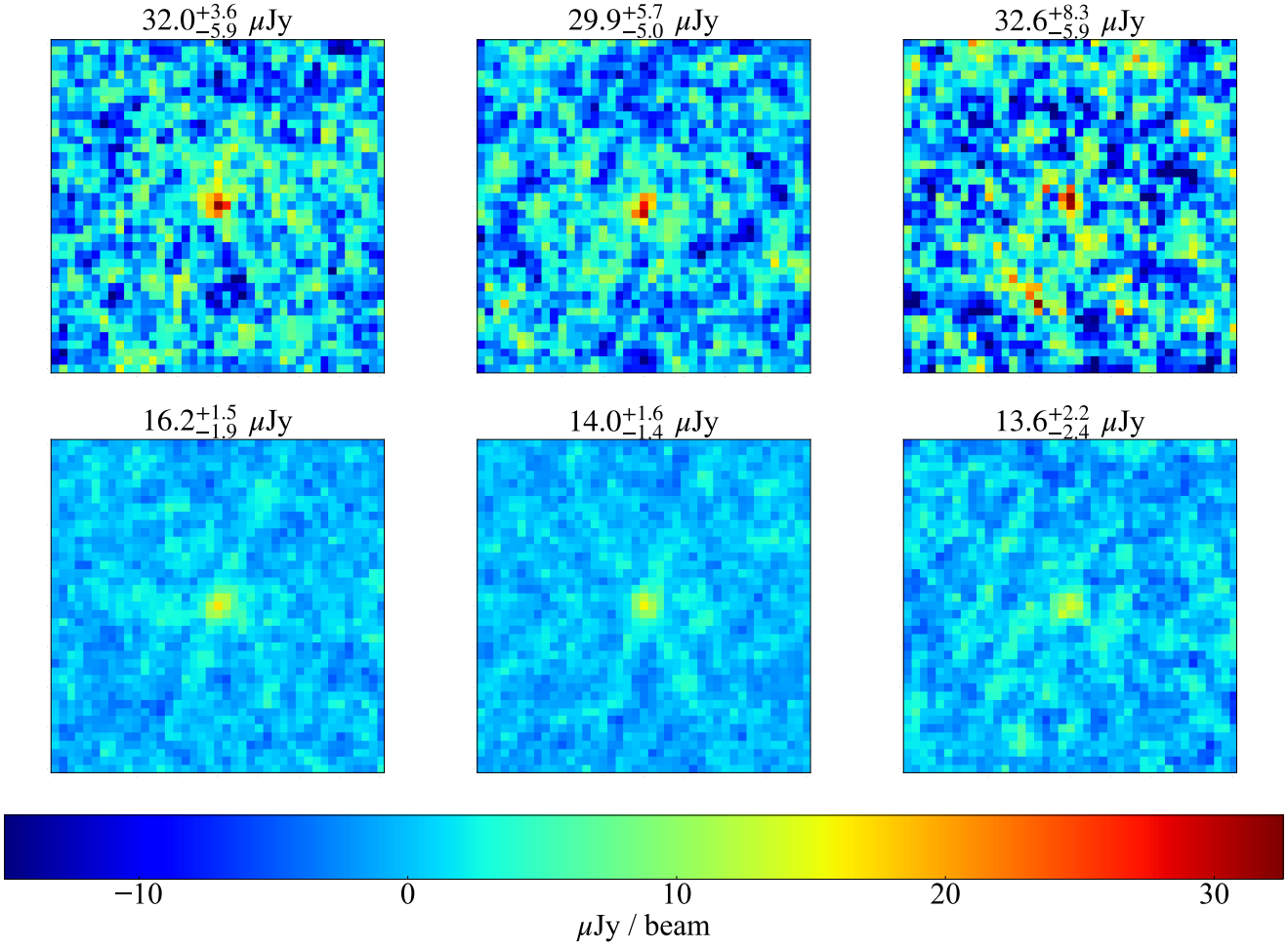

Figure 2. Top row: stacked VLASS images of the AGN in each of the 3 SED bins: faint (left), middle (middle) and bright (right) bins. Bottom row: stacked VLASS images of the control sample of non-AGN galaxies matched in redshift, stellar mass and in star-forming properties. All the co-added images have a scale of 41″ × 41″ with pixel size = 1″.

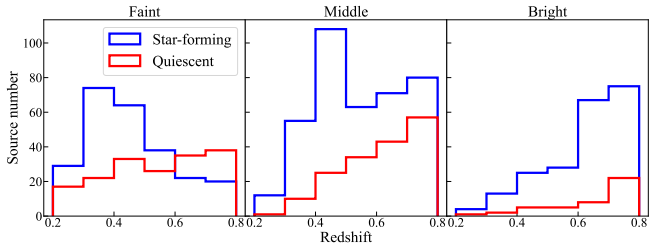

Figure 3. The redshift distributions of the quiescent (red) and star-forming (blue) host galaxies in each luminosity bin.

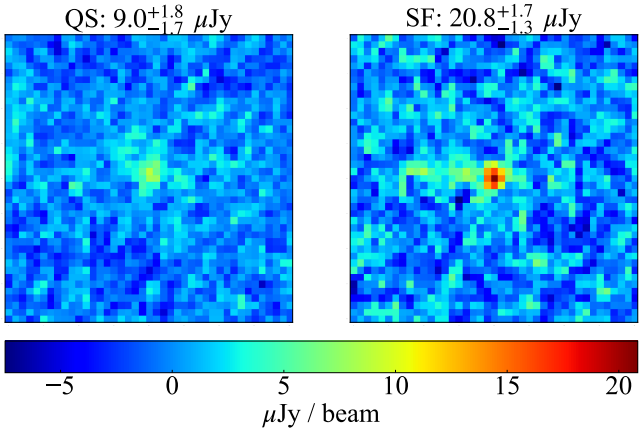

Figure 4. Stacked VLASS images of 4000 quiescent (left) and star-forming (right) inactive galaxies with redshift $0.4 < z < 0.5$ and log $M_{\rm stellar}$ ($M_\odot$) [10.5–11.0].

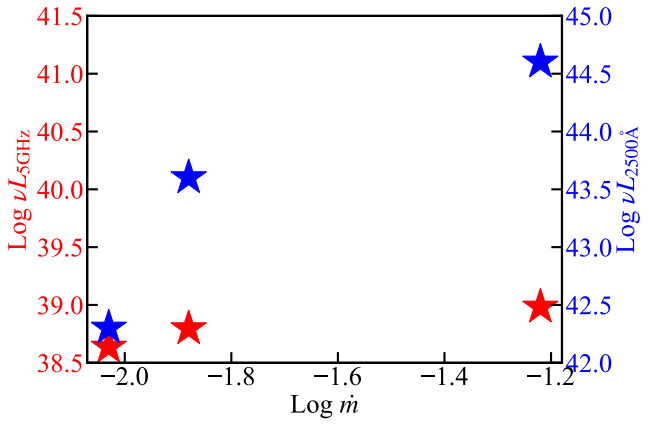

Figure 5. Log $\dot{m}$ versus $\nu L_{2500\text{Å}}$ (blue) and $\nu L_{5\ \rm GHz}$ (red) in the three bins. The UV luminosity is changing by a factor than 100 while radio by a factor 2.

emission, while its accretion rate is ∼ 6× higher and UV emission is ∼ 100× brighter (see Figure 5).

Therefore, we conclude the radio power of AGN is not dependent on the power of the accretion disk or the overall accretion rate. Instead, the relatively constant radio power is more consistent with correlating with the relatively constant X-ray power. Such a correlation is predicted by the 'fundamental plane of black hole activity' (e.g., Merloni et al. 2003; Falcke et al. 2004; Wang et al. 2006; Yuan et al. 2009; Bonchi et al. 2013; Xie & Yuan 2017; Bariuan et al. 2022; Wang et al. 2024). This is an empirical correlation between the X-ray and radio luminosity of stellar and supermassive black holes at varying $\dot{m}$, but has theoretical underpinning if the X-rays are assumed to be from a radiatively inefficient flow, where the accretion power $P_{\rm acc} = \dot{m}M$ but the radiated X-ray flux is $L_{\rm X} \propto \dot{m}P_{\rm acc}$ (as the efficiency increases with $\dot{m}$, Narayan & Yi 1994). This connects to the base of a Blandford & Königl (1979) self-similar conical jet with power $P_{\rm jet} \propto P_{\rm acc}$ (Heinz & Sunyaev 2003). The radio flux is given by the sum of self absorbed synchrotron components from the vertically extended, self similar jet, leading to a flat spectrum in teh radio with monochromatic $L_{\rm R} \propto (\dot{m}M)^{17/12}$ (Blandford et al. 1983; Heinz & Sunyaev 2003; Merloni et al. 2003). Substituting for $\dot{m}$ from the $L_{\rm X}$ relation gives a prediction that $L_{\rm R} \propto (L_{\rm X}M)^{17/24}$ so $\log L_{\rm R} = 0.71 \log L_{\rm X} + 0.71 \log M + C$ where C is a constant. A more detailed (post-diction!) examination of ADAF properties gives $L_{\rm X} \propto \dot{m}^{2.3}M$, matching the observed trend from the data of $\log L_{\rm R} = 0.60 \log L_{\rm X} + 0.78 \log M + C$ (Merloni et al. 2003).

First we simply plot our three bins on the empirical FP relation derived by Merloni et al. (2003). They define $L_{\rm X}$ from the 2–10 keV X-ray luminosity of the hot corona so we integrate our AGN best-fit hot Compontonized model (blue dashed line in Figure 1) over this range. This gives log $L_{\rm X}$ (erg s^{-1}) of 43.51, 43.64 and 43.88, for the faint, middle and bright bin, respectively. We combine this with the radio luminosities in each bin to plot our 3 stacked SEDs on the FP relation in Figure 6. Our three bins are below (radio fainter) by an order of magnitude than predicted by the empirical relationship.

We note the consistency would be slightly better if we had plotted the observed radio fluxes (open stars, see inset in Figure 6 and 7), rather than correcting for the contribution of the host galaxy and indeed Merloni et al. (2003) do not subtract any host galaxy contribution. However, more importantly, Merloni et al. (2003) only use objects which are *detected* in radio flux, so are likely biased high relative to our sample. We test this by showing the 29 individually detected VLASS sources separately on Figure 6, colour coding to distinguish between those in the faint (lightblue diamand), middle (orange pentagon) and bright (green hexagon) bins [1]. There is only one known blazar in the sample (marked with a cross in Figure 6), where the radio is known to be strongly enhanced by Doppler boosting, but all the other individually detected sources are systematically above the Merloni et al. (2003) relation, so it is clear that radio flux limited samples will bias high when the radio detections are incomplete.

We also include data from black hole X-ray binaries, using the 'Radio/X-ray correlation database for X-ray binaries' (Bahramian & Rushton 2022). We assume $M_{\rm BH} = 10M_\odot$ and a power law X-ray spectrum with $\Gamma = 2.0$. We find these binaries, many of which were studied after Merloni et al. (2003), are also slightly radio fainter on average than the original FP. We highlight the original sources in Merloni et al. (2003) in red and see that the BHXRBs population is also slightly below the original FP of Merloni et al. (2003). Therefore, the constant in the FP of Merloni et al. (2003) is likely overestimated.

We explore this further using the (58-month) Swift BAT ultra-hard X-ray flux limited sample of AGN (Mushotzky et al. 2014), where the $z < 0.05$ subset in the North has recently been surveyed at high spatial resolution and high sensitivity with VLA imaging at 22 GHz (Magno et al. 2025). This is an almost complete radio detected subsample,

[1] We use a simple power law with Galactic absorption corrected to fit their eFEDS spectra and calculate the 2–10 keV $L_{\rm X}$. The eROSITA spectra of the several faintest sources are not good enough for a robust fitting (see last few panels of Figure A2), which cause underestimation of their $L_{\rm X}$. The obvious outlier (lightblue diamand with extremly low $L_{\rm X}$) in Figure 6 is source 31206, shown in the last panel of Figure A2.

so should be relatively unbiased. We select the AGN with masses in our range of log $M_{\rm BH} = 8.0 - 8.5$, extrapolate the 22 GHz flux of the core ($1''$ flux) down to 5 GHz assuming a power law $F_\nu \propto \nu^\alpha$ with $\alpha = -0.5$. We show these as brown squares on Figure 7. There are only 2 sources above the FP (PKS2331-240 and Arp102B), the rest are below, but now with individually detected sources rather than a stack. This gives further confidence in the level of radio detected from our stacked sample, as the VLA resolves out all large scale extended star formation in this very low z sample. However, there can still be small scale extended radio emission contaminating the expected compact jet, and higher resolution VLBA images are clearly a better way to explore this (Fischer et al. 2021; Chen et al. 2023).

This dispersion in radio flux *on the FP* (i.e. corrected for X-ray luminosity) is more than a factor 100 for AGN of the same mass and mass accretion rate. Clearly there is at least one other parameter which is important in setting the radio luminosity. Jet power is known to depend strongly on black hole spin, via the Blandford & Znajek (1977) process (Blandford et al. 1983; Tchekhovskoy et al. 2010), so this could be a major source of this dispersion, though the jet power will also depend on the history of accumulation of magnetic flux pinned onto the black hole (Begelman 2012), and/or there may be a supermassive counterpart of the transient discrete ballistic jets which are triggered at the spectral transition in BHXRBs (Nipoti et al. 2005).

These additional processes can enhance the power of the radio emission above that predicted by the FP extended from the stellar mass BHXRBs. The BHXRBs discrete ejections are already excluded from the radio-X-ray correlation, so extrapolating from these sources to the AGN depends on the mean BHXRBs spin and magnetic flux. Spin can be measured in BHXRBs but this is currently controversial (Belczynski et al. 2024; Zdziarski et al. 2024, 2025). Here we assume they have mean spin of around $0.5 - 0.7$ as indicated from fitting a sequence of disc spectra of fixed innermost stable orbit to the disc dominated spectra (Gierliński & Done 2004; Done et al. 2007). AGN spins (and masses) depend on their history of accretion over cosmic time, so they can have a wide range in spin (Volonteri et al. 2005; Beckmann et al. 2025). We assume no net magnetic flux, i.e. the accretion flow is SANE (Zdziarski & Heinz 2024). This predicts that the AGN which are lower relative to the FP are then lower spin than the BHXRBs, while those above have higher spin.

2.4 Fundamental plane versus radio-loudness

The stacked radio from our sample is more or less consistent with an origin in a compact steady jet, which scales in a self similar way with the X-ray hot flow across the mass scale from BHXRBs as predicted by the FP (Merloni et al. 2003). Our AGN sample spans above and below the very obvious spectral transition at $L \sim 0.01 L_{\rm Edd}$, and we find that these are consistent with the same disc-jet coupling, with very little change in either the radio or X-ray luminosity despite a large change (factor 6) in mass accretion rate and an even larger change (factor 100) in UV flux. However, this large change in disc flux does give a large change in the radio to optical/UV ratio which is the classic definition of radio jet power via the radio-loudness parameter.

We define the radio-loudness parameter as $R = L_{5\ \rm GHz}/L_{2500\text{Å}}$. We measure $L_{2500\text{Å}}$ in each of our 3 stacked spectra (Figure 1) and determine $L_{5\ \rm GHz}$ for which $R = 10$. These lines are shown in Figure 7 for the faint (lightblue), middle (orange) and bright (green) bins. The bin width in black hole mass and X-ray luminosity give the extent of the RL/RQ line for the bright and middle bins, but the lowest luminosity SED is extended down to much lower L_x due to the inclusion of lower $\dot{m}$ sources in the BASS sample.

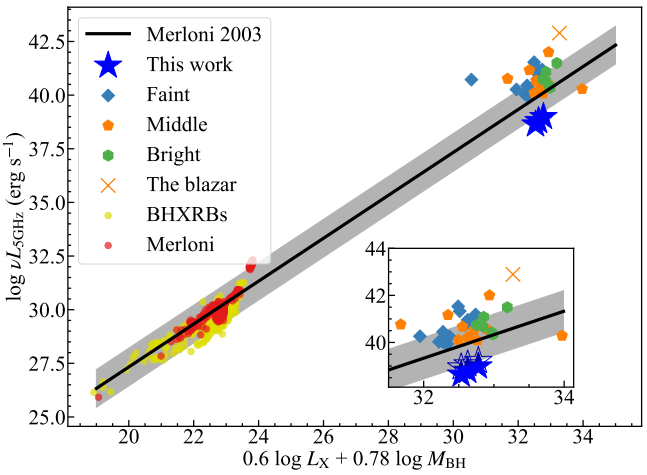

Figure 6. The three luminosity bins of the eFEDS-HSC sample in this work plotted on the fundamental plane of black hole activity extended down to the BHXRBs range (Merloni et al. 2003). $L_{\rm X}$ refers to the rest-frame 2–10 keV luminosity derived by integrating the hot Comptonization component of the best-fit AGNSED model. The inset zooms in to the AGN region for our sample, with the open stars showing the radio luminosities without the subtraction of the host galaxies. We also show the 29 individually detected AGN with colours and shapes indicating their SED bin (faint: lightblue diamand, middle: orange pentagon, bright: green hexagon). The cross marks the one known blazar in the sample. It is very clear that the individually detected objects are brighter with respect to their observed X-ray emission than the stacked undetected ones. We also include BHXRBs with available X-ray and radio data. Red points indicate those in the original sample of Merloni et al. (2003), while yellow are more recent detections.

Our stacked radio from the undetected sources and the bulk of the BASS AGN radio sample for black holes of the same mass lie between the $R = 10$ lines for the faint and middle sample. Thus the majority of these AGN will change classification at the spectral transition from RL (faint) to RQ (middle-bright), yet the radio shows almost no change. The change in designation is driven solely by the change in disc component not the jet itself.

This all supports the discussion above where distance from the FP is taken as a better measure of relative jet power. However, we notice that the $R = 10$ line for bright AGN coincides with the FP for this AGN mass range, illustrating why this single number has been so useful in identifying high power jets. However, it also has clear drawbacks, firstly as illustrated here at the spectral transition, and secondly as it does not correct for the increasing radio dominance expected for the same self absorbed synchrotron spectrum at higher masses (Schulze et al. 2017).

3 DISCUSSION

We show above that the clear spectral transition seen in the stacked eROSITA sample does not impact on the the core radio emission despite the factor 6 change in $\dot{m}$ and factor 100 change in optical/UV flux. The AGN remain on the FP, as their X-ray flux is similarly unaffected by the transition.

This highlights a difference between the AGN and BHXRBs in terms of their X-ray emission above the transition. In BHXRBs, the X-ray coronal flux above the transition can be extremely weak, and current radio flux sensitivity limits make it difficult to follow. Cyg

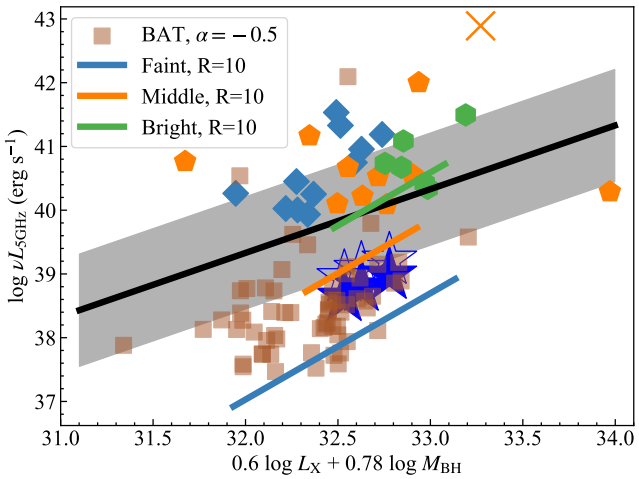

Figure 7. Zoom in of Figure 6 with addional hard X-ray selected AGN from the SWIFT BASS VLA sample for this fixed mass bin of $\log M(M_\odot) = 8.0 - 8.5$ (brown squares). These are a nearby ($z < 0.05$), almost complete radio detected sample, and are observed at high spatial resolution so their radio emission is not contaminated by the host galaxy (Magno et al. 2025). This makes them an excellent comparison set to our stacked, host galaxy subtracted points. The bulk of the BASS sample are consistent with our stacks, but again there is a tail with significantly higher radio emission for the same mass and mass accretion rates. We also mark on the classic $R = 10$ RL/RQ distinction for our three SED bins with coloured solid lines. This shows that our stacks, and the bulk of the BASS AGN, will change from RL to RQ at the spectral transition, not due to any change in the jet but solely driven by the change in disc. Distance away from the FP relation (radio to X-ray ratio) is a much better indicator of the intrinsic jet power than the classic radio loudness (radio to optical/UV ratio).

X-1 is currently the only BHXRBs which can be reliably tracked across the transition due to its distinctive, quite strong X-ray coronal emission in its soft state and its relatively nearby distance. The radio drops dramatically across the transition relative to the lower energy X-ray bandpass where the disc dominates, but this is due to the increase in disc flux (Zdziarski et al. 2011). Instead, the ratio of radio to *coronal* (non-disc) X-ray flux remains on the FP but both radio and coronal X-ray fluxes are lower than in the hard state (Zdziarski & Heinz 2024). A few other BHXRBs have much weaker constraints for their soft state radio and coronal X-ray emission, and these may imply that the radio emission is weaker than predicted by the FP (LMC X-1 and LMC X-3 Gallo et al. 2003, GX339-4: Corbel et al. 2013). Nonetheless, even in Cyg X-1, the radio and coronal X-rays both drop markedly at the spectral transition (Zdziarski et al. 2020), whereas both remain roughly constant in our AGN sample across the same transition. Coronal X-rays are ubiquitous in bright AGN (Brandt & Alexander 2015), unlike the BHXRBs where the disc can completely dominate the luminosity output above the spectral transition.

We speculate that this difference in X-ray (and radio) properties between the stellar and supermassive black holes comes from their very different environments. Stellar mass black holes with low and intermediate mass companions accrete via Roche lobe overflow, so the material has high angular momentum. By contrast, in AGN (and in wind fed high mass X-ray binaries) there can more easily be a larger scale height, lower angular momentum accretion flow as well as a high angular momentum disc. Cyg X-1 may lie in between these two extremes, as it is a high mass binary with a strong stellar wind but almost completely fills its Roche lobe. If the coronal X-ray emission in AGN after the transition is always from a large scale height flow at approximately the maximum ADAF luminosity (Kubota & Done 2018; Mitchell et al. 2023), then the FP correlation is maintained even after the disc formation, as seen here. The FP models are then not only applicable to low luminosity, hard state flows which are radiatively inefficient. They can also extend to bright AGN states above the transition.

4 SUMMARY AND CONCLUSIONS

We recently demonstrated that AGN show a similar state transition to the stellar mass BHXRBs using stacked SEDs built from the combination of the eFEDS-HSC. This is a sample of X-ray selected, unobscured AGN with host galaxy subtraction from HSC imaging. Selecting only those with similar host galaxy masses, and using this to determine black hole mass, gave a sequence of uniformly selected AGN spectra with $\dot{m} \sim 0.01$ to $\dot{m} \sim 0.3$. This clearly shows a dramatic increase in the optically thick disc component in the UV across the transition at $\sim 0.01 L_{\mathrm{Edd}}$.

Here we investigate how the compact radio jet responds to this transition by stacking the VLASS radio images of our eFEDS-HSC sample. The flux limits on our sample mean that any individually detected source is classed as RL, while those with only upper limits are likely RQ. We only have 29 detected sources out of a total of 1305 AGN, so we remove these and stack the remaining undetected ones, reducing to three bins of $\dot{m}$ to obtain enough signal-to-noise. We find that each bin is significantly detected in radio emission at approximately similar flux levels. We correct for extended radio emission from the host galaxies by subtracting a matched sample of non-AGN, matched also in the ratio of quiescent and starforming galaxies with the same stellar mass. This is responsible for only around half of the detected emission. The remaining radio flux remains remarkably constant across the three bins, despite these spanning the spectral transition, with mass accretion rate increasing by a factor 6 and optical/UV increasing by a factor 100. However, the X-ray flux is likewise remarkably constant across the three SED bins, and the radio/X-ray ratio of all three are consistent with lying on the FP, i.e. consistent with the expected scaling up in mass of the compact, steady jet seen in the BHXRBs. This is confirmed in a very different AGN sample of ultra-hard X-ray selected SWIFT BAT AGN. We use only the AGN in our mass range of $\log M = 8.0 - 8.5$ and find that these individual, nearby, extremely well resolved AGN have radio/X-ray points which lie on top of the ratios derived from our stacked spectra.

This shows that both the stellar mass and supermassive black holes show similar disc-jet coupling, or rather X-ray flow-jet coupling. Both systems have radio which follows the optically thin, X-ray hot coronal flux and not the optically thick, cool disc component. However, it also highlights a difference which is that in BHXRBs the disc can almost completely dominate above the transition, with very little coronal flux, whereas in AGN above the transition the X-ray corona is always present with luminosity which seems to be quite close to the maximal ADAF luminosity. We speculate that this is due to a separate large scale height flow in AGN from lower angular momentum material which is not present in the Roche lobe overflow BHXRBs.

Our data also highlight the well known dispersion in radio properties of AGN, with a factor 100 difference in radio luminosity even on the FP. We highlight how the classical radio-loudness parameter (ratio of radio to optical/UV emission) is not a good tracer of the jet emission at the transition as R increases due to the drop in optical disc flux, changing from RQ to RL for no change in radio jet flux. We suggest distance from the fundamental plane (ratio of observed radio

flux to that predicted by the FP) is a better measure of jet power, and speculate that this is a measure of black hole spin.

ACKNOWLEDGEMENTS

We thank Andrzej A. Zdziarski, Leah Morabito and Macon Magno for useful discussions on this paper. JK gratefully acknowledges the scholarship of University of Science and Technology of China for a visiting program to Durham University. JK and JW acknowledges support from the National Natural Science Foundation of China (grant Nos. 123B2042). SH acknowledges support from the Japan Society for the Promotion of Science (JSPS) through the short-term fellowship PE23722 and from the Science and Technologies Facilities Council (STFC) through the studentship grant ST/W507428/1. CD acknowledges support from STFC through grant ST/T000244/1 and Kavli IPMU, University of Tokyo. Kavli IPMU was established by World Premier International Research Center Initiative (WPI), MEXT, Japan. JS is supported by JSPS KAKENHI (23K22533) and the World Premier International Research Center Initiative (WPI), MEXT, Japan. This work was supported by JSPS Core-to-Core Program (grant number: JPJSCCA20210003). MJT is supported by STFC through grant ST/X001075/1.

This research has made use of the CIRADA cutout service at URL cutouts.cirada.ca, operated by the Canadian Initiative for Radio Astronomy Data Analysis (CIRADA). CIRADA is funded by a grant from the Canada Foundation for Innovation 2017 Innovation Fund (Project 35999), as well as by the Provinces of Ontario, British Columbia, Alberta, Manitoba and Quebec, in collaboration with the National Research Council of Canada, the US National Radio Astronomy Observatory and Australia's Commonwealth Scientific and Industrial Research Organisation.

This work is based on data from eROSITA, the soft X-ray instrument aboard SRG, a joint Russian-German science mission supported by the Russian Space Agency (Roskosmos), in the interests of the Russian Academy of Sciences represented by its Space Research Institute (IKI), and the Deutsches Zentrum für Luft- und Raumfahrt (DLR). The SRG spacecraft was built by Lavochkin Association (NPOL) and its subcontractors, and is operated by NPOL with support from the Max Planck Institute for Extraterrestrial Physics (MPE). The development and construction of the eROSITA X-ray instrument was led by MPE, with contributions from the Dr. Karl Remeis Observatory Bamberg & ECAP (FAU Erlangen-Nuernberg), the University of Hamburg Observatory, the Leibniz Institute for Astrophysics Potsdam (AIP), and the Institute for Astronomy and Astrophysics of the University of Tübingen, with the support of DLR and the Max Planck Society. The Argelander Institute for Astronomy of the University of Bonn and the Ludwig Maximilians Universität Munich also participated in the science preparation for eROSITA. The authors gratefully acknowledge Andrea Merloni's contribution to the eROSITA project in general and this sample in particular. This research has made use of the VizieR catalogue access tool, CDS, Strasbourg, France.

DATA AVAILABILITY

The eFEDS-HSC sample is from Hagen et al. (2024), and the inactive galaxy sample of Kawinwanichakij et al. (2021) is available at https://member.ipmu.jp/john.silverman/HSC/. VLASS images are available at https://archive-new.nrao.edu/vlass/quicklook/ and cutouts at cutouts.cirada.ca.

REFERENCES

Aihara H., et al., 2022, PASJ, 74, 247
Bahramian A., Rushton A., 2022, bersavosh/XRB-LrLx_pub: update 20220908, doi:10.5281/zenodo.7059313, https://doi.org/10.5281/zenodo.7059313
Bariuan L. G. C., Snios B., Sobolewska M., Siemiginowska A., Schwartz D. A., 2022, MNRAS, 513, 4673
Beckmann R. S., et al., 2025, MNRAS, 536, 1838
Begelman M. C., 2012, MNRAS, 420, 2912
Behar E., Baldi R. D., Laor A., Horesh A., Stevens J., Tzioumis T., 2015, MNRAS, 451, 517
Belczynski K., Done C., Hagen S., Lasota J.-P., Sen K., 2024, A&A, 690, A21
Blandford R. D., Königl A., 1979, ApJ, 232, 34
Blandford R. D., Znajek R. L., 1977, MNRAS, 179, 433
Blandford R. D., Applegate J. H., Hernquist L., 1983, MNRAS, 204, 1025
Bonchi A., La Franca F., Melini G., Bongiorno A., Fiore F., 2013, MNRAS, 429, 1970
Bonzini M., et al., 2015, MNRAS, 453, 1079
Brandt W. N., Alexander D. M., 2015, A&ARv, 23, 1
Brunner H., et al., 2022, A&A, 661, A1
Calistro Rivera G., et al., 2024, A&A, 691, A191
Chen S., Laor A., Behar E., Baldi R. D., Gelfand J. D., 2023, MNRAS, 525, 164
Chen S., et al., 2024, ApJ, 975, 35
Condon J. J., 1992, ARA&A, 30, 575
Corbel S., Coriat M., Brocksopp C., Tzioumis A. K., Fender R. P., Tomsick J. A., Buxton M. M., Bailyn C. D., 2013, MNRAS, 428, 2500
Delvecchio I., et al., 2017, A&A, 602, A3
Done C., Gierliński M., Kubota A., 2007, A&ARv, 15, 1
Falcke H., Biermann P. L., 1995, A&A, 293, 665
Falcke H., Körding E., Markoff S., 2004, A&A, 414, 895
Fawcett V. A., Alexander D. M., Rosario D. J., Klindt L., Fotopoulou S., Lusso E., Morabito L. K., Calistro Rivera G., 2020, MNRAS, 494, 4802
Fender R. P., Belloni T. M., Gallo E., 2004, MNRAS, 355, 1105
Fernández-Ontiveros J. A., Muñoz-Darias T., 2021, MNRAS, 504, 5726
Fischer T. C., et al., 2021, ApJ, 906, 88
Gallo E., Fender R. P., Pooley G. G., 2003, MNRAS, 344, 60
Ghisellini G., Tavecchio F., Foschini L., Ghirlanda G., Maraschi L., Celotti A., 2010, MNRAS, 402, 497
Gierliński M., Done C., 2004, MNRAS, 349, L7
Giroletti M., Panessa F., 2009, ApJ, 706, L260
Hagen S., et al., 2024, MNRAS, 534, 2803
Heinz S., Sunyaev R. A., 2003, MNRAS, 343, L59
Jana A., et al., 2025, A&A, 693, A35
Jiang L., Fan X., Ivezić Ž., Richards G. T., Schneider D. P., Strauss M. A., Kelly B. C., 2007, ApJ, 656, 680
Kang J.-L., Done C., Hagen S., Temple M. J., Silverman J. D., Li J., Liu T., 2025, MNRAS, 538, 121
Karim A., et al., 2011, ApJ, 730, 61
Kawinwanichakij L., et al., 2021, ApJ, 921, 38
Kellermann K. I., Sramek R., Schmidt M., Shaffer D. B., Green R., 1989, AJ, 98, 1195
Körding E. G., Jester S., Fender R., 2006, MNRAS, 372, 1366
Kubota A., Done C., 2018, MNRAS, 480, 1247
Lacy M., et al., 2020, PASP, 132, 035001
Laor A., Behar E., 2008, MNRAS, 390, 847
Li J., et al., 2024, MNRAS, 527, 4690
Liao M., Wang J., Kang W., Zhou M., 2022, MNRAS, 512, 296
Liao M., Wang J., Ren W., Zhou M., 2024, MNRAS, 528, 3696
Liu T., et al., 2022, A&A, 661, A5
Maccarone T. J., 2003, A&A, 409, 697
Magno M., et al., 2025, ApJ, 981, 202
Merloni A., Heinz S., di Matteo T., 2003, MNRAS, 345, 1057
Mitchell J. A. J., Done C., Ward M. J., Kynoch D., Hagen S., Lusso E., Landt H., 2023, MNRAS, 524, 1796

Moravec E., Svoboda J., Borkar A., Boorman P., Kynoch D., Panessa F., Mingo B., Guainazzi M., 2022, A&A, 662, A28
Mushotzky R. F., Shimizu T. T., Meléndez M., Koss M., 2014, ApJ, 781, L34
Narayan R., Yi I., 1994, ApJ, 428, L13
Nims J., Quataert E., Faucher-Giguère C.-A., 2015, MNRAS, 447, 3612
Nipoti C., Blundell K. M., Binney J., 2005, MNRAS, 361, 633
Noda H., Done C., 2018, MNRAS, 480, 3898
Padovani P., 2016, A&ARv, 24, 13
Panessa F., Giroletti M., 2013, MNRAS, 432, 1138
Panessa F., Baldi R. D., Laor A., Padovani P., Behar E., McHardy I., 2019, Nature Astronomy, 3, 387
Planck Collaboration et al., 2020, A&A, 641, A6
Ruan J. J., Anderson S. F., Eracleous M., Green P. J., Haggard D., MacLeod C. L., Runnoe J. C., Sobolewska M. A., 2019, ApJ, 883, 76
Sargent M. T., et al., 2010, ApJS, 186, 341
Schulze A., Done C., Lu Y., Zhang F., Inoue Y., 2017, ApJ, 849, 4
Sobolewska M. A., Siemiginowska A., Gierliński M., 2011, MNRAS, 413, 2259
Svoboda J., Guainazzi M., Merloni A., 2017, A&A, 603, A127
Tchekhovskoy A., Narayan R., McKinney J. C., 2010, ApJ, 711, 50
Temple M. J., et al., 2023, MNRAS, 518, 2938
Thean A., Pedlar A., Kukula M. J., Baum S. A., O'Dea C. P., 2001, MNRAS, 325, 737
Urry C. M., Padovani P., 1995, PASP, 107, 803
Vahdat Motlagh A., Kalemci E., Maccarone T. J., 2019, MNRAS, 485, 2744
Volonteri M., Madau P., Quataert E., Rees M. J., 2005, ApJ, 620, 69
Wang R., Wu X.-B., Kong M.-Z., 2006, ApJ, 645, 890
Wang Y., Wang T., Ho L. C., Zhong Y., Luo B., 2024, A&A, 689, A327
White R. L., Helfand D. J., Becker R. H., Glikman E., de Vries W., 2007, ApJ, 654, 99
Xie F.-G., Yuan F., 2017, ApJ, 836, 104
Yuan F., Yu Z., Ho L. C., 2009, ApJ, 703, 1034
Yue B. H., et al., 2024, MNRAS, 529, 3939
Yun M. S., Reddy N. A., Condon J. J., 2001, ApJ, 554, 803
Zakamska N. L., Greene J. E., 2014, MNRAS, 442, 784
Zakamska N. L., et al., 2016, MNRAS, 455, 4191
Zdziarski A. A., Heinz S., 2024, ApJ, 967, L7
Zdziarski A. A., Skinner G. K., Pooley G. G., Lubiński P., 2011, MNRAS, 416, 1324
Zdziarski A. A., Shapopi J. N. S., Pooley G. G., 2020, ApJ, 894, L18
Zdziarski A. A., Banerjee S., Chand S., Dewangan G., Misra R., Szanecki M., Niedźwiecki A., 2024, ApJ, 962, 101
Zdziarski A. A., Banerjee S., Szanecki M., Misra R., Dewangan G., 2025, ApJ, 981, L15
Zeltyn G., et al., 2024, ApJ, 966, 85

APPENDIX A: SED AND VLASS IMAGES OF INDIVIDUAL SOURCES

This paper has been typeset from a TEX/LATEX file prepared by the author.

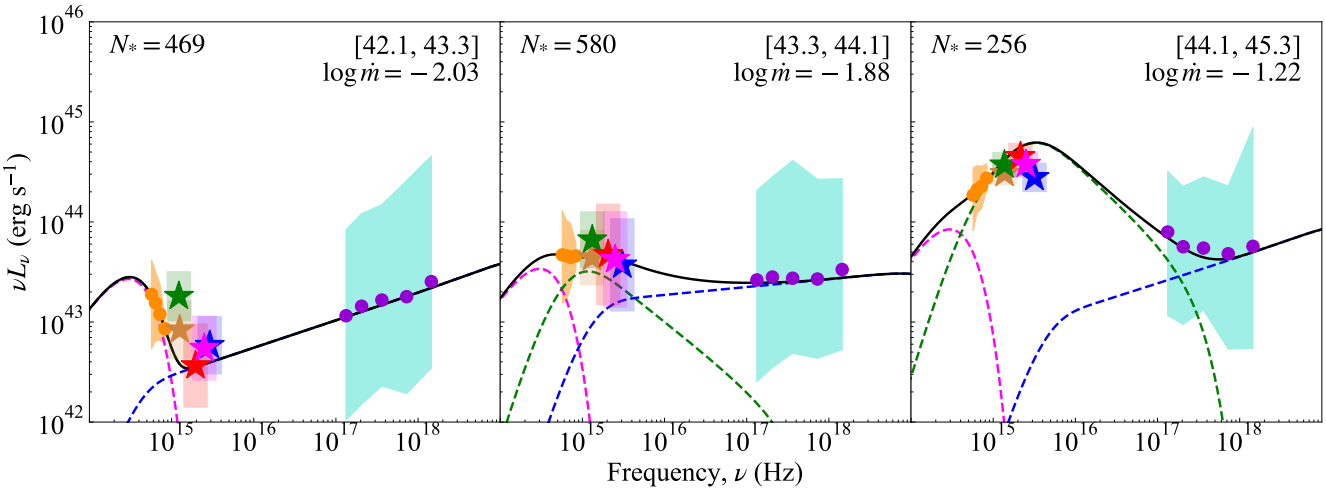

Figure A1. The stacked optical to X-ray SED in the three bins derived by averaging those in Hagen et al. (2024) and Kang et al. (2025). The SED points are from low to high frequency: HSC (orange points), SDSS *u*-band (green star), KiDS *u*-band (brown star), GALEX NUV (red star), GALEX 1200Å (magenta star), GALEX FUV (blue star) and eROSITA (purple points). See Hagen et al. (2024) and Kang et al. (2025) for additional details.

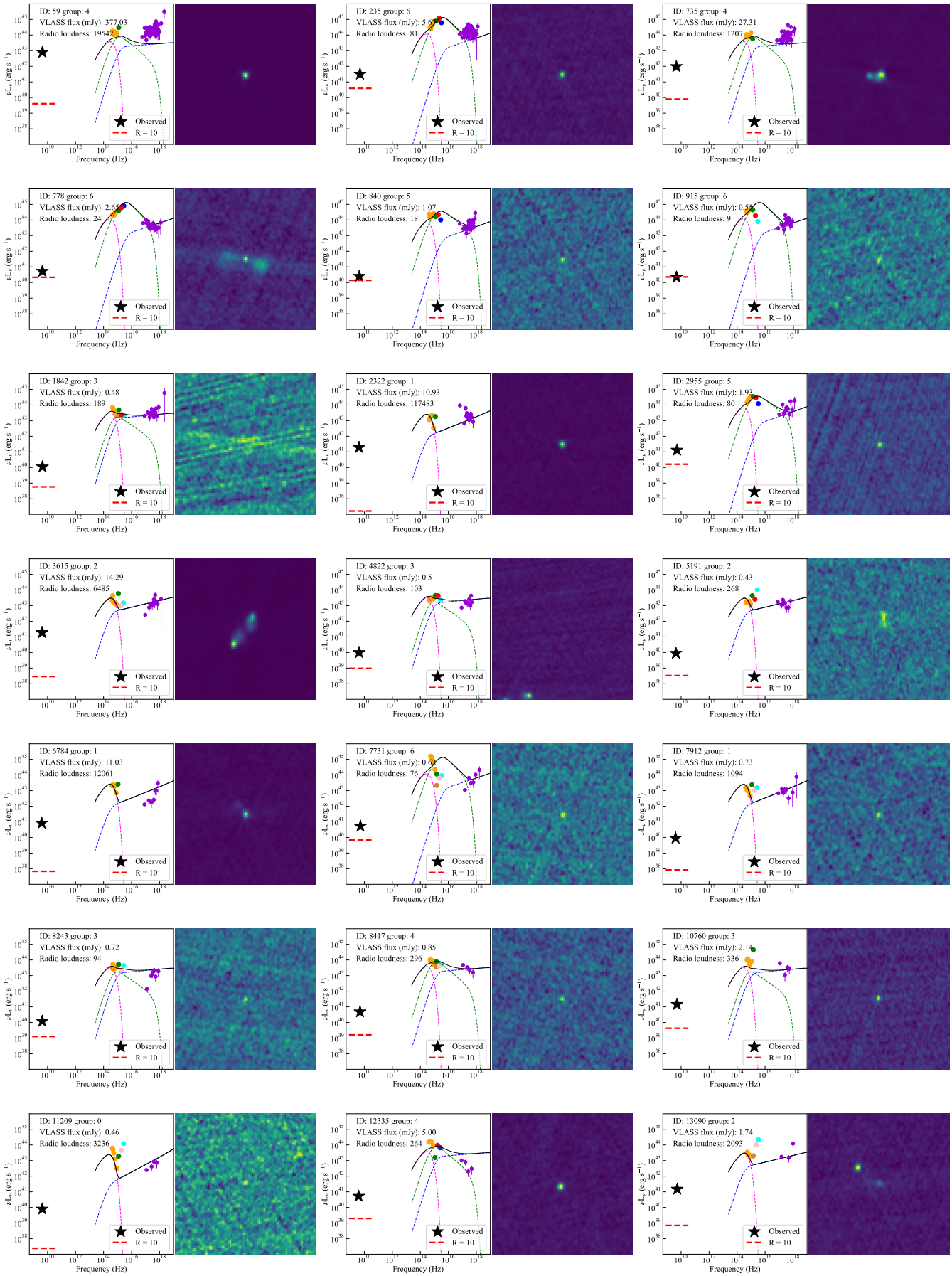
ID: 59 group: 4
VLASS flux (mJy): 377.03
Radio loudness: 19542
ID: 235 group: 6
VLASS flux (mJy): 5.67
Radio loudness: 81
ID: 735 group: 4
VLASS flux (mJy): 27.31
Radio loudness: 1207
ID: 778 group: 6
VLASS flux (mJy): 2.64
Radio loudness: 24
ID: 840 group: 5
VLASS flux (mJy): 1.07
Radio loudness: 18
ID: 915 group: 6
VLASS flux (mJy): 0.55
Radio loudness: 9
ID: 1842 group: 3
VLASS flux (mJy): 0.48
Radio loudness: 189
ID: 2322 group: 1
VLASS flux (mJy): 10.93
Radio loudness: 117483
ID: 2955 group: 5
VLASS flux (mJy): 1.93
Radio loudness: 80
ID: 3615 group: 2
VLASS flux (mJy): 14.29
Radio loudness: 6485
ID: 4822 group: 3
VLASS flux (mJy): 0.51
Radio loudness: 103
ID: 5191 group: 2
VLASS flux (mJy): 0.43
Radio loudness: 268
ID: 6784 group: 1
VLASS flux (mJy): 11.03
Radio loudness: 12061
ID: 7731 group: 6
VLASS flux (mJy): 0.62
Radio loudness: 76
ID: 7912 group: 1
VLASS flux (mJy): 0.73
Radio loudness: 1094
ID: 8243 group: 3
VLASS flux (mJy): 0.72
Radio loudness: 94
ID: 8417 group: 4
VLASS flux (mJy): 0.85
Radio loudness: 296
ID: 10760 group: 3
VLASS flux (mJy): 2.14
Radio loudness: 336
ID: 11209 group: 0
VLASS flux (mJy): 0.46
Radio loudness: 3236
ID: 12335 group: 4
VLASS flux (mJy): 5.00
Radio loudness: 264
ID: 13090 group: 2
VLASS flux (mJy): 1.74
Radio loudness: 2093
Observed
R = 10
Frequency (Hz)
νL_ν (erg s^{-1})

Figure A2.

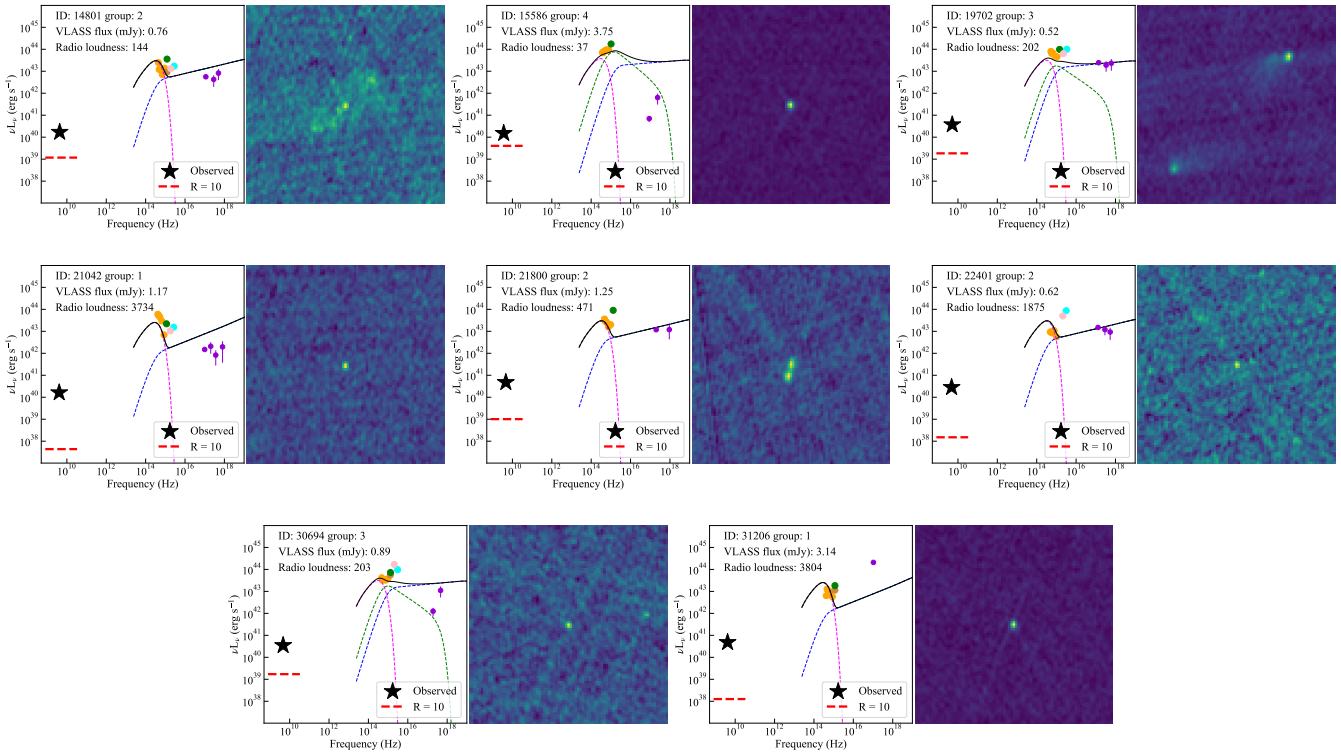

Figure A2. Full SEDs of the individually detected VLASS sources (left) and the VLASS images (right). Pale red (blue) points mark the detected NUV (FUV) photometries of GALEX, while pink (cyan) mark the upper limits. The IDs are the *ID_SRC* in the eFEDS AGN catalog (Liu et al. 2022). The group number refers to the bins in Hagen et al. (2024); [0, 1, 2] correspond to the faint, [3, 4] to the middle, and [5, 6, 7] to the bright bins in this paper. Most (21/29) of our sources are compact. There are 5 images showing clear evidence for extended jet lobes (IDs 778 3615 14801 19702 21800) and 4 where there the radio morphology is extended but unclear (IDs 735 1842 5191 6784). The radio flux is taken from the single pixel peak central flux, so is weighted to the core flux even where there are obvious extended structures, though the core flux of IDs 3615 is likely contaminated by the extended emission. The red star on the SED marks $R = 10$, the classical definition of a RL source, while the black star shows the level of detected radio luminosity. The VLASS flux limit of $\sim 420\mu$Jy corresponds to $\sim 10^{40}$ ergs s^{-1} for the mean source redshift here. All the VLASS images have a scale of $81'' \times 81''$ with pixel size = $1''$.

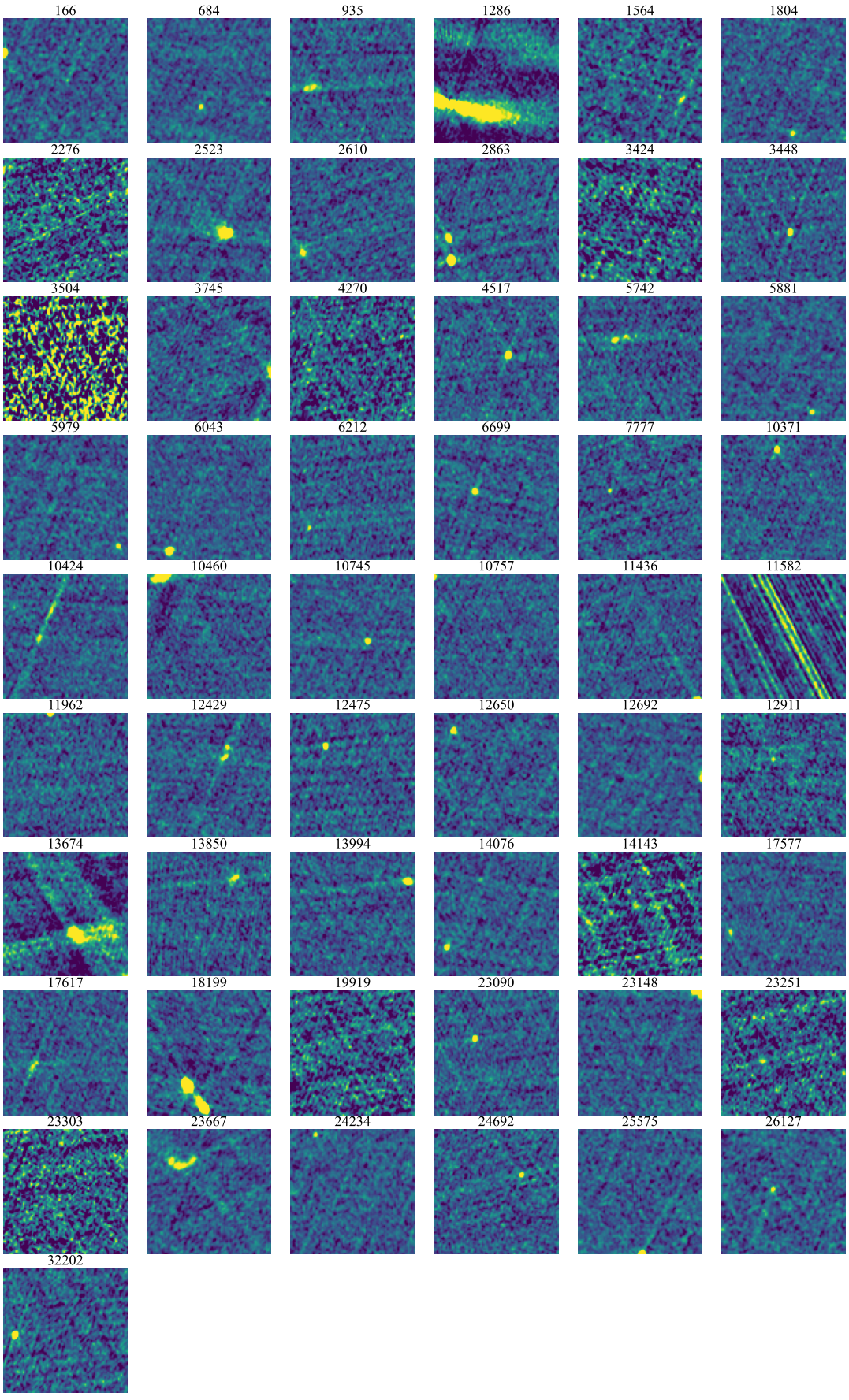

Figure A3. VLASS images of the sources dropped from the sample due to identified counterparts being clearly offset sources and/or image contamination.